Geophysical Journal International

Geophys. J. Int. (2024) **237,** 557–569
Advance Access publication 2024 February 20
GJI Rock and Mineral Physics, Rheology

https://doi.org/10.1093/gji/ggae058

High-resolution source imaging and moment tensor estimation of acoustic emissions during brittle creep of basalt undergoing carbonation

Tong Bai [1], Tiange Xing [1], Matěj Peč [1] and Nori Nakata [1,2]

[1] *Department of Earth, Atmospheric and Planetary Sciences, Massachusetts Institute of Technology, Cambridge, MA* 02139*, USA. E-mail: tbai@mines.edu*
[2] *Energy Geosciences Division, Lawrence Berkeley National Laboratory, Berkeley, CA* 94720*, USA*

Accepted 2024 February 19. Received 2024 January 30; in original form 2023 March 15

SUMMARY

As the high-frequency analogue to field-scale earthquakes, acoustic emissions (AEs) provide a valuable complement to study rock deformation mechanisms. During the load-stepping creep experiments with CO_2-saturated water injection into a basaltic sample from Carbfix site in Iceland, 8791 AE events are detected by at least one of the seven piezoelectric sensors. Here, we apply a cross-correlation-based source imaging method, called geometric-mean reverse-time migration (GmRTM) to locate those AE events. Besides the attractive picking-free feature shared with other waveform-based methods (e.g. time-reversal imaging), GmRTM is advantageous in generating high-resolution source images with reduced imaging artefacts, especially for experiments with relatively sparse receivers. In general, the imaged AE locations are found to be scattered across the sample, suggesting a complicated fracture network rather than a well-defined major shear fracture plane, in agreement with X-ray computed tomography imaging results after retrieval of samples from the deformation apparatus. Clustering the events in space and time using the nearest-neighbour approach revealed a group of 'repeaters', which are spatially co-located over an elongated period of time and likely indicate crack, or shear band growth. Furthermore, we select 2196 AE events with high signal-to-noise-ratio (SNR) and conduct moment tensor estimation using the adjoint (backpropagated) strain tensor fields at the locations of AE sources. The resulting AE locations and focal mechanisms support our previously assertion that creep of basalt at the experimental conditions is accommodated dominantly by distributed microcracking.

Key words: Creep and deformation; Acoustic emission; Induced seismicity.

1 INTRODUCTION

Mitigation of human-induced climate change necessitates capture and storage of CO_2 to prevent further rise of global temperatures. One possible strategy is to inject CO_2-rich fluids into mafic and ultramafic rocks, which contain abundant divalent cations such as Ca^{2+} and Mg^{2+} that can react with the injected fluids and form solid carbonate minerals (e.g. $CaCO_3$, $MgCO_3$; Lackner *et al.* 1995). This mineralization approach has been successfully applied at the CarbFix site in Iceland since 2012 resulting in rapid carbon mineralization and permanent carbon storage over geological timescales (Matter *et al.* 2016). Injection of large fluid volumes will be necessary to offset the approximately 40 Gt of CO_2 emitted annually (IPPC 2.5 °C report). Fluid injection modifies the stress state in the reservoir and can induce deformation and seismicity that needs to be managed. It is therefore critical to improve our understanding of deformation of mafic and ultramafic rocks in the presence of reactive fluids inducing various dissolution-precipitation reactions and ultimately leading to carbon mineralization.

Deformation at typical reservoir pressure and temperature conditions amenable to mineralization is dominated by brittle phenomena such as fracturing, frictional sliding and cataclastic flow. Of particular interest is 'brittle creep' deformation, also referred to as 'static fatigue', which is commonly observed in all types of rocks (e.g. Scholz 1968; Atkinson & Meredith 1987; Heap *et al.* 2011; Brantut *et al.* 2012) as an important mechanism during long-term rock deformation. Brittle creep allows crack propagation at a stress below the critical fracture toughness of rocks and is activated by a chemically sensitive process called stress corrosion (Ashby & Sammis 1990). Minor changes to the stress state or fluid chemistry can lead to rapid growth and interconnection of the cracks ultimately resulting in large-scale failure along faults, potentially inducing seismicity and endangering the stability of the reservoir. Brittle creep phenomena are typically modelled as occurring on

inclined shear cracks that nucleate tensile cracks at their tips as they slide, interacting with surrounding flaws during growth (so-called wing-crack/sliding-crack model, Ashby & Sammis 1990; Brantut *et al.* 2012; Bernabé & Pec 2022). Resolving the location, timing, fracture mode and impulsiveness of these growing and interacting flaws is therefore useful for studying brittle creep.

Acoustic emission (AE) monitoring is one of the most popular *in situ* imaging methods for studying brittle phenomena in laboratory rock deformation experiments during which the elevated temperature and pressure conditions often prohibit direct observation. An AE occurs when a rapid stress drop in a localized zone generates an elastic wave. Theoretically, any rapid defect motion can generate AEs. In practice, only a small portion of defects emit recordable AEs due to the limited sensor sensitivity and frequency range any data acquisition system can record (e.g. Lockner 1993; Zang *et al.* 1998; Ghaffari & Pec 2020; O'Ghaffari *et al.* 2023). The 'loudest' events are typically associated with microcracking, yet only a small portion of cracks emit recordable AEs in laboratory settings (Lockner 1993). Nevertheless, direct AE event counting and relevant statistical analysis (e.g. *b*-value) provides most straightforward indication of the rock deformation process (Kiyoo 1962; Goodman 1963). Locating AE events represents a leveraged level of study that reflects their temporal and spatial patterns (Manthei & Eisenblätter 2008). AE imaging and analysis has been widely used in the experimental studies of rock deformation and provided insights on the mechanism underlying fracturing and faulting (e.g. Meredith & Atkinson 1983; Lockner *et al.* 1991, 1992; Baud & Meredith 1997; Benson *et al.* 2007; Goebel *et al.* 2012; Brantut 2018).

In general, AE source localization improves with the amount of receivers recording the event. Current state-of-the art approaches to locating AEs necessitate a broad sensor coverage (12–16 sensors) which allows for an accuracy of about 1–2 mm in source location (e.g. Brantut 2018; Petružálek *et al.* 2018). However, such complete sensor coverage competes for limited space on the sample surface with other sensors such as strain gauges necessitating large samples. Reliable source location techniques that can work also with a smaller sensor coverage would be therefore useful. Furthermore, most of the AE location methods used are based on traveltime information (Benson *et al.* 2007; Dong *et al.* 2020), which can be easily biased by picking errors (Benson *et al.* 2007). Free from arrival time picking, waveform-based imaging methods (e.g. time-reversal imaging or TRI) prove to be more robust for locating events with low signal-to-noise (SNR) data and/or for locating synchronized events. In conventional TRI (Fink 1997), or arithmetic-mean reverse-time migration (AmRTM; Nakata & Beroza 2016), the data are reversed in the time axis before being simultaneously injected at the corresponding receivers. With sufficiently accurate velocity model and wide acquisition apertures, the backpropagated wavefields are supposed to focus at the original spatio-temporal location. However, with sparse receivers in some AE experiments, especially those at elevated temperatures and pressures, TRI often suffers from strong artefacts caused by insufficient receiver wavefield sampling. Besides, the onset time estimation of TRI (especially for 3-D images) is non-trivial which further adds the uncertainty of source location estimation.

To overcome these challenges, Nakata & Beroza (2015) and Sun *et al.* (2015) proposed the geometric-mean reverse-time migration (GmRTM), which replaces the wavefield summations from TRI with cross-correlations. Effective in producing high-resolution source images with fewer imaging artefacts, GmRTM enables stacking over time and circumvents the tedious onset time search. The trade-off is the substantial increase in computational cost since GmRTM breaks the linear-superposition law and consequently requires separate wavefield propagation at each receiver. Combining the conventional AmRTM and GmRTM, a hybrid GmRTM scheme (Sun *et al.* 2015; Bai *et al.* 2022b) strikes a balance between image resolution and computational cost, and provides a more feasible option for real-data applications.

In addition to the estimated source locations, the AE source mechanism analysis can further facilitate crack characterization, for example, estimating orientation and other mechanical properties, during the loading process (e.g. Ohtsu 1991; Chang & Lee 2004; Aker *et al.* 2014). Based on the arithmetic-mean values of the recorded first-motion polarities, Zang *et al.* (1998) define three crack types: type-S (shear), type-T (tensile) and type-C (collapse), and conduct source analysis in granite cores. Using Zang's method, Lei *et al.* (2000) categorize cracks as type-S, type-T, type-TS (a slip along the crack with tensile cracking at the end), and type-TTS (combination of two type-TS cracks) in a hornblende schist. Despite its simplicity and computational efficiency, the average-polarity method has restrictions on the inferred source types (Graham *et al.* 2010). Taking advantage of the first-motion amplitude information, the moment tensor inversion (MTI) method (Ohtsu 1991; Chang & Lee 2004; Manthei 2005; Petružálek *et al.* 2018; Jia *et al.* 2022) can provide more detailed source information, for example, associated volume change, source orientation and opening directions, etc, (Graham *et al.* 2010).

Acting as approximate solutions to the inverse problems, the adjoint operations (Tromp *et al.* 2005; Fichtner *et al.* 2006) can sometimes perform better than the inversion operators (Claerbout 2014) and are widely used in seismology community, for example, for gradient computation in full-waveform inversion (Virieux & Operto 2009; Plessix 2006). Similarly, the traditional MTI methods can be approximated by their adjoint operation, the TRI or back-projection method (Kawakatsu & Montagner 2008), as has been applied on several microseismic data sets (Gharti *et al.* 2011; Vlček *et al.* 2016; Finger & Saenger 2021).

In this study, we have applied the GmRTM method to locate AEs and analyse the moment tensor on data obtained from laboratory rock deformation study of brittle creep (Xing *et al.* 2022). Xing *et al.* (2022) performed long-term creep experiments with CO_2-rich aqueous pore fluid on a basalt sample from the Carbfix field and, based on the mechanical and microstructural observations, concluded that distributed microcracking is the dominant deformation mechanism. The observed time dependence of strain accumulation at constant stress is likely caused by subcritical crack growth in the presence of the reactive fluids. Here, we complement the study of Xing *et al.* (2022) with source location and focal mechanism analysis using GmRTM and elastic time-reversal method, respectively, and try to improve the understanding of the underlying deformation mechanisms that facilitate long-term brittle creep in a porous basalt undergoing carbonation.

2 DATA AND METHOD

2.1 Material

The sample material was from a drill core collected at the Carbfix site (e.g. Gislason *et al.* 2010) from a formation called the Hellishedi basalt at a depth of ∼350 m, and ground to a right rectangular cylinder with ∼ 40 mm in diameter and 80 mm in length (Xing *et al.* 2022). The rock has an average porosity of 8 per cent

according to the hydrological and tracer recovery modelling (Alfredsson *et al.* 2008; Matter & Kelemen 2009; Aradóttir *et al.* 2012; Snæbjörnsdóttir & Gislason 2016). Laboratory measurements using Archimedes' method and CT (Computed Tomography) data show an average porosity of 5–15 per cent as displayed in Fig. 1, in broad agreement with porosity estimates from field data (Gislason *et al.* 2010). The pores are spherical and approximately equi-dimensional with a mean diameter of ∼400 μm frequently filled with secondary alteration minerals and potassium feldspar. The rock is formed by an aphanitic matrix that consists of crystals of feldspar laths (with a mean length of approximately 150 μm and an aspect ratio of 10:1), interstitial clinopyroxene and olivine (with a mean grain size of approximately 35 μm) with frequent dendritic morphology. The presence of glass and secondary alteration minerals such as smectite and zeolite is commonly observed (Fig. 1). More details about the starting material microstructure can be found in Xing *et al.* (2022).

2.2 Data acquisition and pre-processing

Seven piezoelectric sensors were installed around the sample to allow the acquisition of compressional waves during the deformation experiment as presented in Fig. 2. Note that we only analyse AEs occurring during creep at constant stress and exclude any AEs that occur during the imposed load steps. The experiment was performed at a temperature of ∼80 °C with an effective pressure of 50 MPa. The load-stepping method was adopted where during each step cycle, a constant load was kept for ∼24 hr, while deformation of the sample was monitored (see details in Xing *et al.* 2022). In total, 12 creep steps were achieved before the sample failed at 131 MPa differential stress.

With continuous monitoring, the SNR in a moving-time window at the selected master channel is used for AE event detection. Once exceeding a pre-defined threshold, two combined four-channel universal serial bus (USB) oscilloscopes start to record the data at 50 MS s^{-1} with a 12-bit resolution (Xing *et al.* 2022). During the entire experiment, a total of 8791 AE events are detected and recorded during the time when stress is held constant (see Fig. 3 for AE data examples). The signal was amplified using low-noise amplifiers (ITASCA) with a flat gain of 60 dB in a frequency range of 50 kHz to 1.5 MHz (for further details on the ultrasound probe array, see Ghaffari & Pec 2020).

For data pre-processing, we remove the mean and the trend of the data before conducting bandpass filtering in the frequency range of 50 and 500 kHz. Among the seven sensors, sensor no. 3 (Figs 2c and d) at the top is characterized with extremely low-SNR data (Figs 3c and d) due to a different sensor setup. Including such data proves to compromise the imaging result, and hence is rejected in our source location and moment tensor estimation implementations. In the remaining channels, strong coda waves (e.g. reflections) are still frequently observed. Hence, we further multiply the data with its corresponding STA/LTA (short-time average over long-time average) ratios (Akazawa 2004), which helps suppress the coda waves and highlights the primary arrivals (Fig. 3). The lengths of the STA and LTA window are 10 and 180 samples (or 0.8 and 14.4 μs), respectively.

Our sensors are calibrated using laser Doppler vibrometer and the recordings reflect the values of particle velocity (Ghaffari *et al.* 2021), which are then converted to displacement through time integration for the moment tensor estimation. Using the estimated AE source locations, we correct for the sensor directivity (e.g. Aker *et al.* 2014) assuming a cosine sensitivity function. After that, the one-component vector (along the source-sensor line) is decomposed into three (Z-, E- and N-) components in Cartesian coordinate, which is suitable for adjoint elastic wave propagation (see eq. 3 below).

2.3 Geometric-mean reverse-time migration

Conventional TRI highlights the coherence of the overall wavefield at the source location by stacking each different receiver wavefield $R_i(\mathbf{x}, t)$:

$$I(\mathbf{x}, t) = \sum_{i=1}^{N} R_i(\mathbf{x}, t), \tag{1}$$

where t and $\mathbf{x}$ are time and spatial variables, respectively, N denotes the number of receivers and $R_i(\mathbf{x}, t)$ denotes the ith backpropagated wavefield (displacement or pressure or particle velocity) using the corresponding time-reversed data. In practice, a scan over the time axis for the maximum amplitude or best focusing is needed to determine the onset time t_0, at which we extract the source image $I(\mathbf{x}, t_0)$.

For acquisition systems with sparse receivers, summation is often not sufficiently effective in suppressing the imaging artefacts and highlighting the source area, which in turn challenges the excitation time estimation. A cross-correlation-based imaging condition, or the GmRTM (Nakata & Beroza 2016) proves to be effective in generating high-resolution source images with fewer artefacts under this scenario:

$$I(\mathbf{x}) = \sum_{t} \prod_{i=1}^{N} R_i(\mathbf{x}, t). \tag{2}$$

Eq. (2) requires no t_0 estimation, which makes GmRTM more efficient in determining source spatial locations than AmRTM (eq. 1). Still, the temporal information of sources can be obtained by adopting partial stacking (Sun *et al.* 2015) in eq. (2).

2.4 Adjoint wave propagation for moment tensor estimation

With estimated source locations, we proceed to estimate the moment tensor elements to further characterize the sources. As more than six sensors are usually required to stabilize the MTI algorithm (Chang & Lee 2004), we instead adopt the adjoint-state method for estimating focal mechanisms, which tolerates a larger degree of data imperfections (Claerbout 2014). Note that GmRTM can be used directly for MTI (Zhang *et al.* 2023), but again, we need denser networks to stabilize the inversion.

The forward simulation for a point source in elastic media can be written as:

$$\rho\ddot{\mathbf{u}} - \nabla \cdot (\mathbf{c} : \nabla \mathbf{u}) = -\mathbf{M} \cdot \nabla \delta(\mathbf{x} - \mathbf{x_s}) S(t), \tag{3}$$

where ρ and $\mathbf{c}$ denote the density and stiffness tensor, respectively, and $\mathbf{u}$ is the displacement. On the right (source side), $\mathbf{M}$ is the seismic moment tensor, $\delta(\mathbf{x} - \mathbf{x}_s)$ and $S(t)$ denote the spatial δ-function and source time function, respectively.

The gradients of the conventional $l2$-norm objective function with respect to the moment tensor elements M_{ij} can be derived with the adjoint-state method (Jarillo Michel & Tsvankin 2017):

$$\Delta M_{ij} = -\int_0^T \epsilon_{ij}^{\dagger}(\mathbf{x_s}, t) S(T - t) \mathrm{d}t, \tag{4}$$

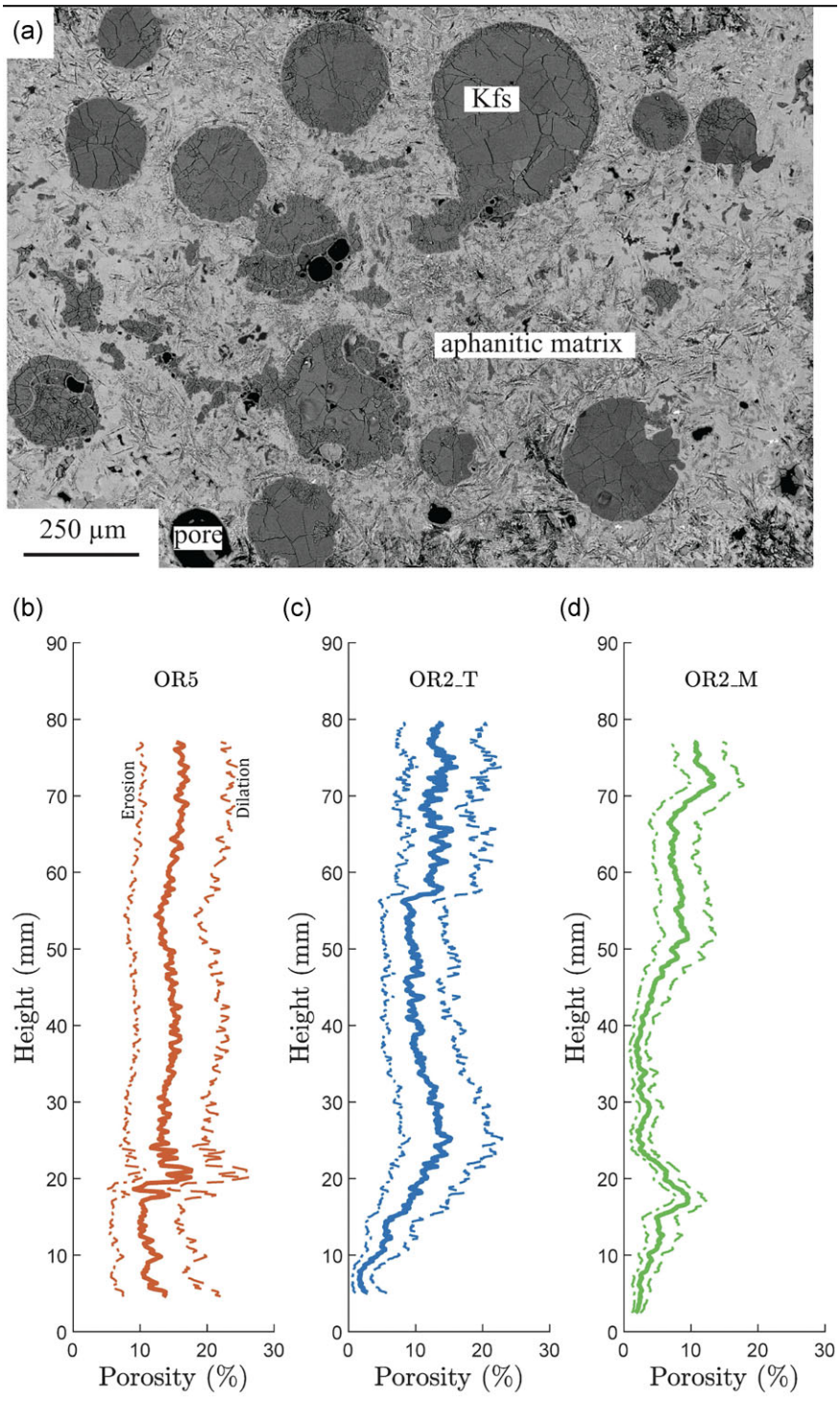

Figure 1. Starting material microstrucutre and porosity distribution. (a) Scanning electron microscope backscattered electron image. Some primary pores are filled with potassium feldspar (Kfs), while others are empty. Aphanitic matrix consists of plagioclase, pyroxene and olivine. (b)–(d) Porosity profiles retrieved from CT scans of three separate basalt cores by grey-level thresholding. Thick lines—mean porosity, and thin lines—error estimates by dilating and contracting the images by 1 pixel, respectively.

where $\boldsymbol{\epsilon}^{\dagger}$ is the adjoint strain tensor and T denotes the recording time. Eq. (4) implies the relative magnitudes of moment tensor elements can be approximated by the adjoint strain tensors at the spatio-temporal locations of AE sources. The feasibility of applying the adjoint-state method for moment tensor estimation is verified with a set of synthetic tests (Fig. S5, Supporting Information), where we reconstructed the moment tensor elements of a point source at 27 different locations across three heights in the sample.

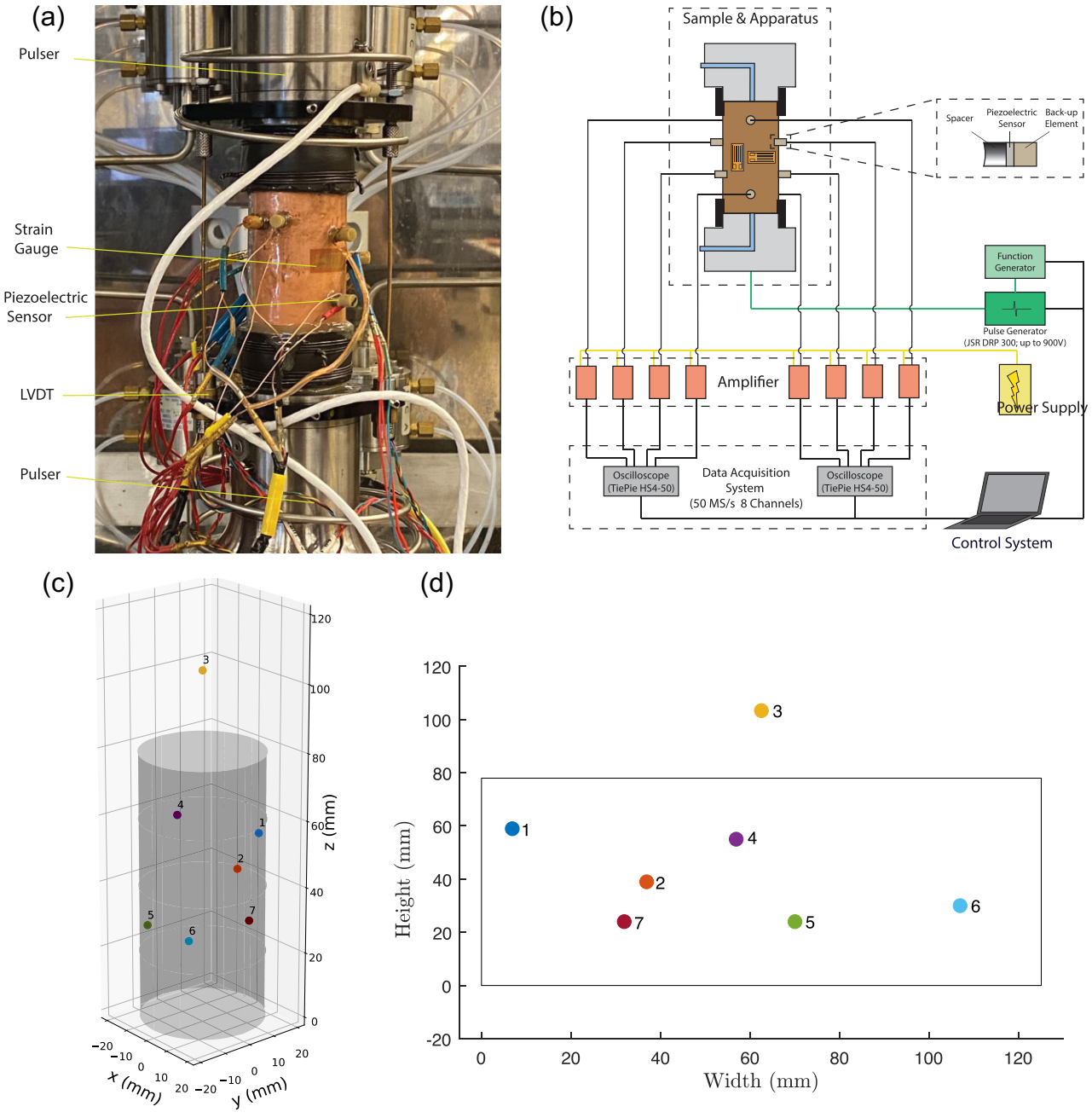

Figure 2. The AE acquisition system: (a) photo of the sample assembly. (b) Sketch of the AE recording system. (c) and (d) Depicts the sensor locations. Panels (a) and (b) are modified from Xing *et al.* (2022).

3 RESULTS

3.1 AE events distribution from imaging

The locations of the 8791 AE events extracted from the corresponding GmRTM image cubes (such as those in Fig. 4) are displayed in Fig. 5. Some horizontal heat maps at different heights (Fig. 5b) are selected to highlight the AE location densities. Note that the spatial resolution is set as 1 mm due to the high computational cost of the 3-D imaging. While the general distribution of located AEs shows no localization, denser AE distributions are observed especially at heights of 36–50 mm in the northwest quadrant (Fig. 5b). However, temporal distribution does not show similar clustering (Fig. 6).

The deformed rock sample was scanned and reconstructed using X-ray computed tomography with scan parameters of ∼150 kV and ∼250 μA (Xing *et al.* 2022). Fig. 7 shows a horizontal and a vertical cross-section from the X-ray tomographic image (with a pixel size of ∼90 ×90 μm) of the deformed sample, overlaid by the traced fractures (yellow lines) and the located AEs (black dots) using GmRTM. Overall, the dense fracture networks from the X-ray image are reasonably well-matched with the high-density AEs depicted in the heat map. However, certain traced fractures located at the bottom and upper left section of the vertical cross-section (Fig. 7b) are not reflected in the AE distribution. This discrepancy may be attributed to the limited acquisition geometry and the 'invisibility' of certain AEs associated with those fractures. If subcritical microcracking is

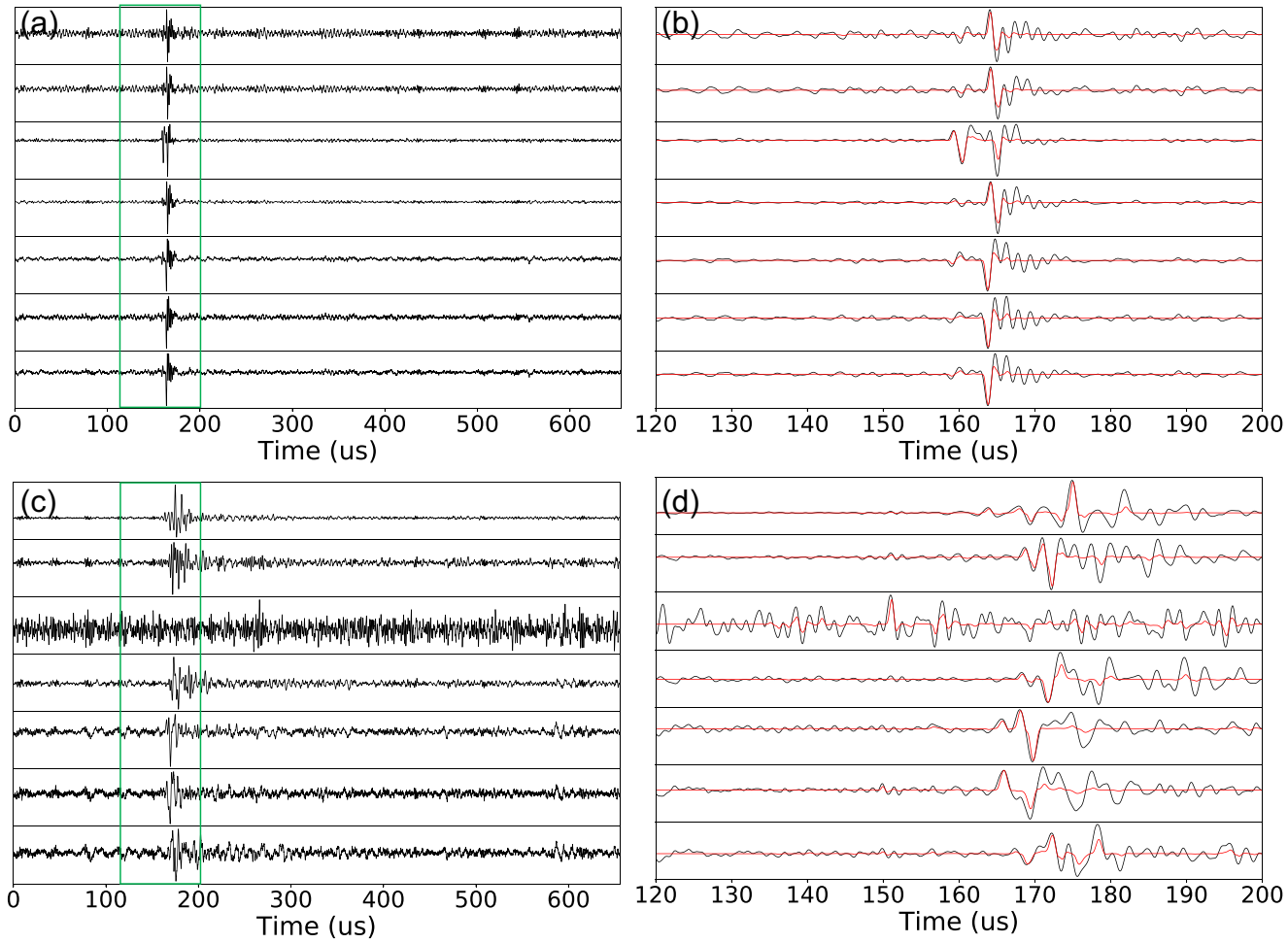

Figure 3. (a) and (b) Two sets of bandpass-filtered seismograms recording three AE events. (c) and (d) The zoomed-in (120–200 μs) counterparts. Black: the filtered data; and red: data additionally multiplied by the STA/LTA ratios.

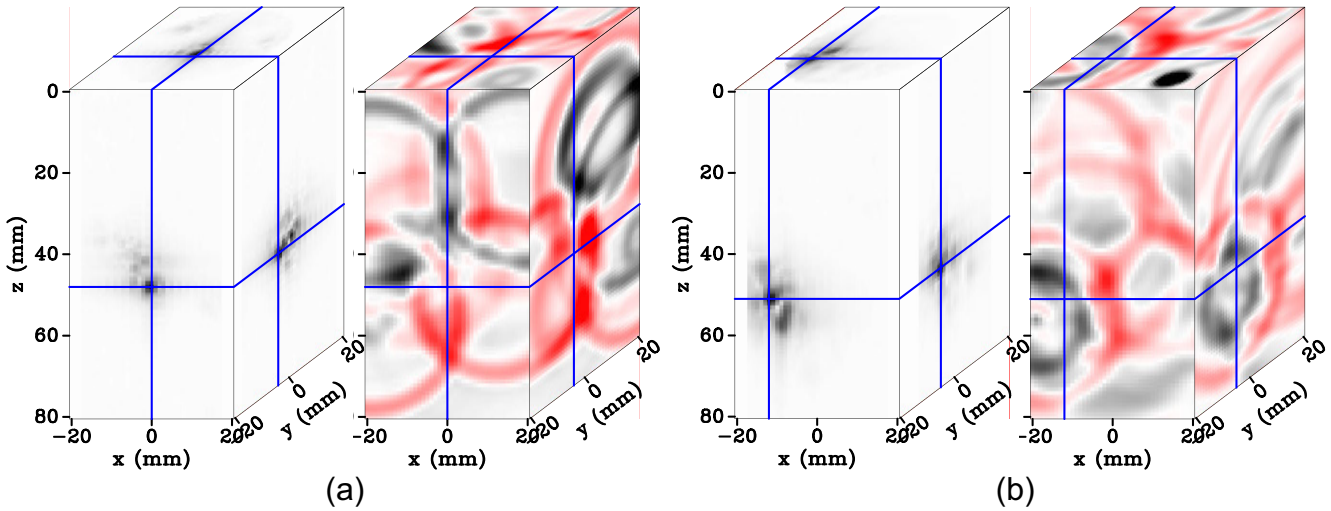

Figure 4. Image cubes corresponding to the sample AE events in (a) Fig. 3(a) and (b) Fig. 3(b). Each subplot compares the GmRTM image (left) and the AmRTM image (right). The blue lines mark the locations of the 2-D slices, which intersect with the source location estimated using GmRTM.

responsible for time-dependent strain accumulation as previously inferred, a large portion of growing cracks might be propagating without emitting acoustic waves.

The AE distributions at each loading stage (Fig. 6) also show a distributed nature. Here, the recorded AEs are grouped by the loading steps with time lapse after each loading encoded by colour. The

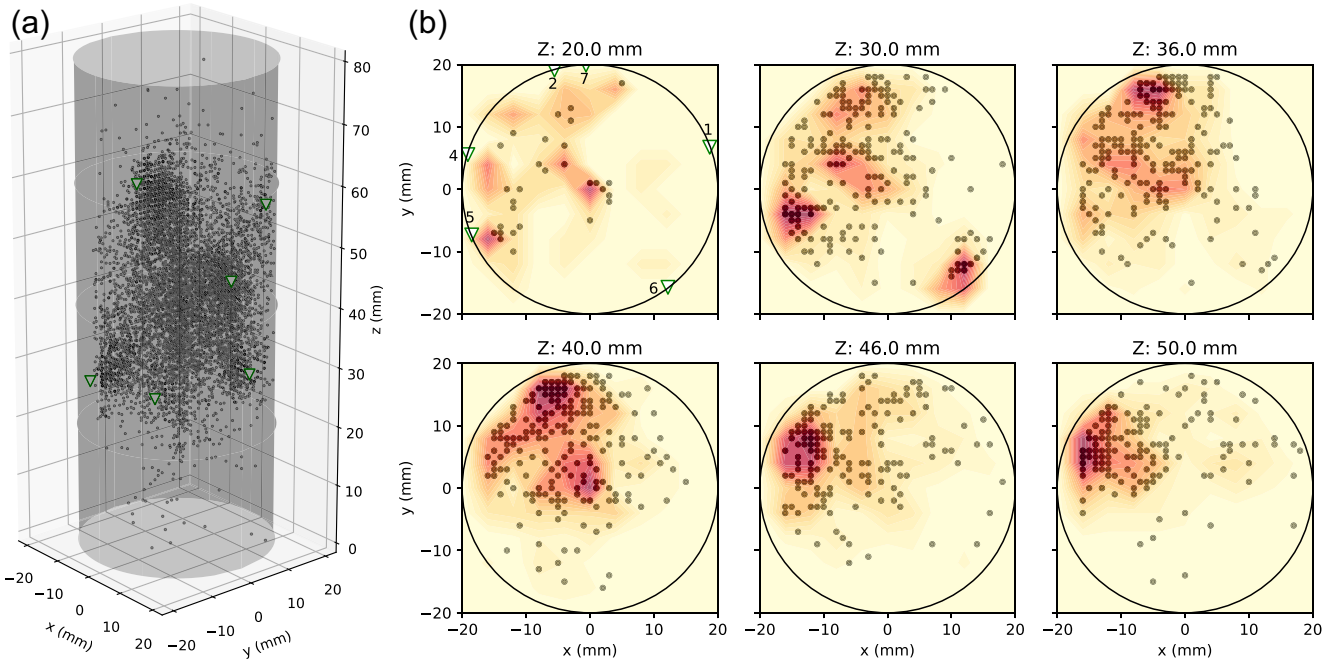

Figure 5. (a) The distributions of all the AEs (black dots) across the specimen and (b) selected horizontal slices, overlaid by heat maps highlighting the density of AE distribution. The projection of the imaged source locations (black dots) is restricted to those within 1 mm from the corresponding slice heights. The green triangles denote the projected location of sensors.

amount of detected AEs at different stages varies, but the spatial-temporal distribution of all the located AEs appears to be random and shows no localization across all stages, that is, we do not observe an evolving fault growth pattern towards the final failure as common in short-term failure experiments (e.g. Lockner *et al.* 1991; Benson *et al.* 2007).

The tempo-spatial distribution of the AE events can be classified into two groups: background events and repeaters (Fig. 8), using the nearest-neighbour approach (Zaliapin & Ben-Zion 2020). Specifically, the AE events are sorted by the so-called nearest-neighbour proximity, which combines the temporal and spatial distances. The 'backgroud' events take place in close temporal distance, while showing large variation in spatial distribution. Therefore these events are likely random 'background' events and are unlikely correlated to each other. While those from the other category, take place in close spatial proximity but occur over an extended period of time and are named 'repeaters', which can be interpreted as the impulsive growth of existing cracks. As expected, the repeaters occur more frequently at later loading stages.

3.2 Focal mechanism estimation

For moment tensor estimation, we select 2196 AE events whose median (over the seven channels) SNR exceeds 20. Here, the SNR is defined as the ratio of the root-mean-square value of the signal window over that of the preceding noise window, both with the window width of 20 μs. Using the backpropagation of the elastic wave equation, we extract the (adjoint) strain tensors at the tempo-spatial locations to approximate the corresponding moment tensors (eq. 4). By decomposing the 3×3 tensor, we computed the fractions of the double-couple (C_{DC}), isotropic (C_{ISO}) and compensated linear vector dipole (C_{CLVD}) components following Vavryčuk (2015). The corresponding crack types can be classified as shear with $C_{\mathrm{DC}} > 60$ per cent, tensile with $C_{\mathrm{DC}} < 40$ per cent, or mixed-mode (shear-tensile) with 40 per cent $\leq C_{\mathrm{DC}} \leq 60$ per cent (Chang & Lee 2004).

We observe no clear relationship between the spatial distribution of AE sources and the estimated fracture types (see the beachballs in Fig. S6, Supporting Information), which supports our conclusion that the deformation under our experimental conditions in general is distributed rather than localized. To further demonstrate this inference, we section the sample and plot the identified cracks at three different height bins: 24–32, 32–40 and 40–48 mm (Fig. 9). Despite some areas with higher crack density (e.g. tensile cracks at height 24–32 mm and shear cracks at 32–48 mm), the overall distribution of AE events is scattered throughout the sample. Furthermore, these subsampled events display a randomized pattern of temporal distribution (Fig. 9). The 3-D plots (Figs 10a and c) imply a similarly scattered spatial-temporal distribution of AE events corresponding to different crack types. Besides, their spatial distribution correlates reasonably well with the fracture and porosity network estimated from the X-ray tomographic image (Fig. 10d).

The focal mechanism analysis reveals that the tensile- and mixed-mode fractures account for ∼58 per cent of the 2196 total examined events (Fig. 11). The proportion of the mixed-mode fractures remains relatively constant throughout the experiment, while the proportion of tensile fractures peaks at around ∼100 hr and then decreases to 36 per cent by the end of the experiment. Conversely, the fraction of shear fractures is lowest at ∼100 hr, but increases thereafter. The focal mechanism results also show a shift in the dominant crack type towards the final failure, where shear fractures

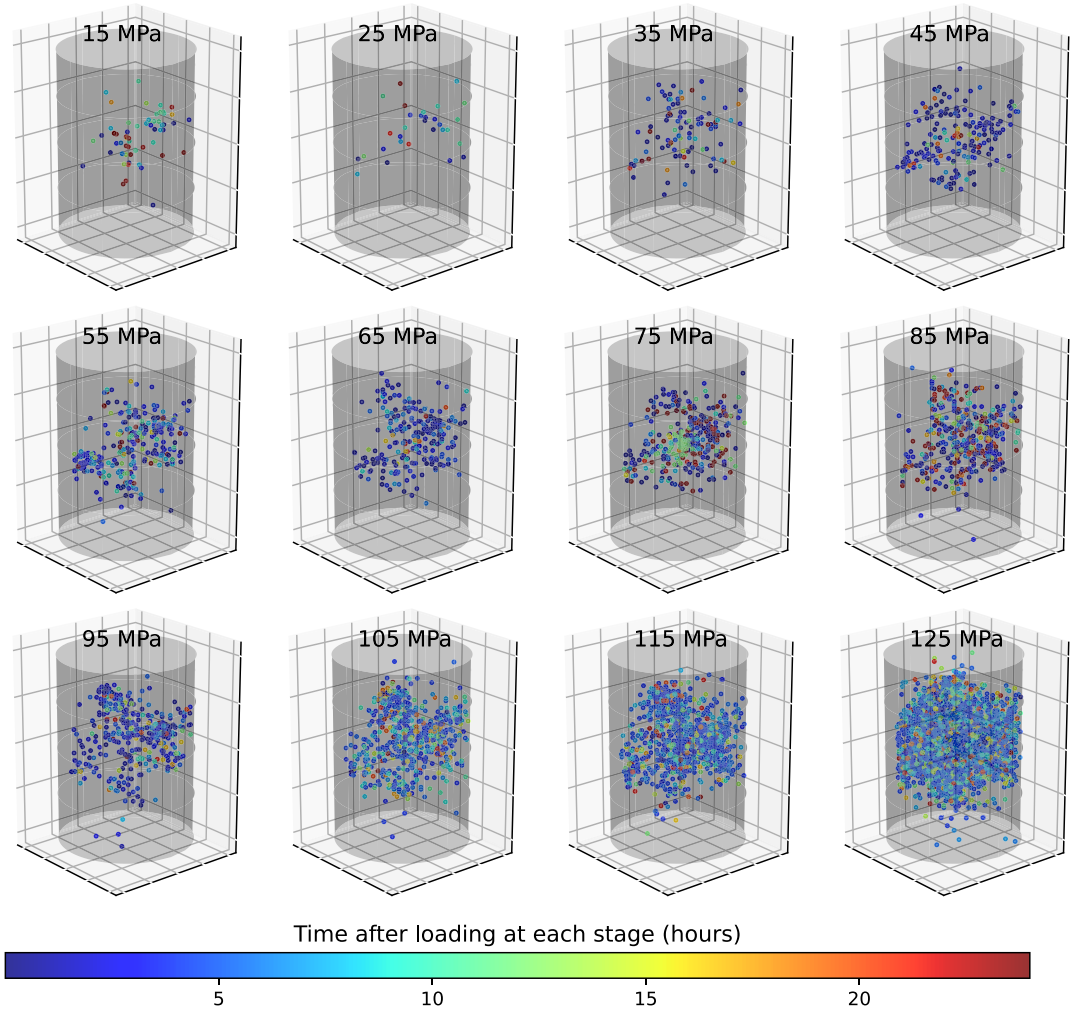

Figure 6. The distributions of AEs at different loading stages, indicated by the differential stresses at the top of each panel. At each stage, the colour encodes the evolving time of 24 hr.

ultimately prevail after ∼245 hr (Fig. 11). Reches (1999) summarized based on previous observations (Lockner *et al.* 1991; Reches & Lockner 1994) that during early stage of the deformation cracks dilate but do not interact with each other, until later when the sample is weakened due to the high crack density and eventually yields by shear. That conclusion is consistent with our focal mechanism analysis that the shear fractures only become dominant at later stage of the deformation when crack coalescence becomes more frequent. Stanchits *et al.* (2006) also observed similar switch in the dominant fracture mode towards failure where the occurrence of shear-type events increases substantially largely at the expense of tensile events. Kwiatek *et al.* (2014) examined temporal changes of seismic moment tensors and *b*-values of AEs and also concluded that large shear-type events becomes dominant as deformation approaching localized failure.

Statistics on the distribution of the maximum waveform amplitude (Fig. 11c) imply similar patterns for the three types of fractures (tensile, shear and mixed) at every amplitude level. That is to say, the distribution pattern of fracture type is similar at different SNR level, that is, resampling based on SNR would not affect the observed pattern. Therefore, the selected 2196 high SNR events out of 8791 recordings are representative of all the AEs recorded during the experiment.

4 DISCUSSION

4.1 GmRTM versus AmRTM (or time-reversal imaging)

We employ acoustic GmRTM for source location and elastic AmRTM for moment tensor estimation. A similar sequential workflow was previously proposed by Finger & Saenger (2021) who utilized the maximum intensity imaging condition (as described in their eq. 6) and elastic AmRTM, respectively. The conventional AmRTM requires focusing-time picking, which can be challenging, especially for 3-D source location problems. In comparison, GmRTM or the maximum density imaging condition simplifies the process by collapsing the time axis and reducing the dimension from 4-D to 3-D. Additionally, the source locations obtained from elastic AmRTM results may not always be associated with the maximum intensity, hindering automatic processing (Artman *et al.* 2010). GmRTM is less impacted by such polarity issues when locating sources in both acoustic or elastic media (Nakata & Beroza 2016; Bai *et al.* 2022a). In this study, we used acoustic rather than elastic GmRTM for source location, primarily for computational efficiency.

Posing more strict requirements of data quality, moment tensor estimation is often applied on a subset of the total detected AE

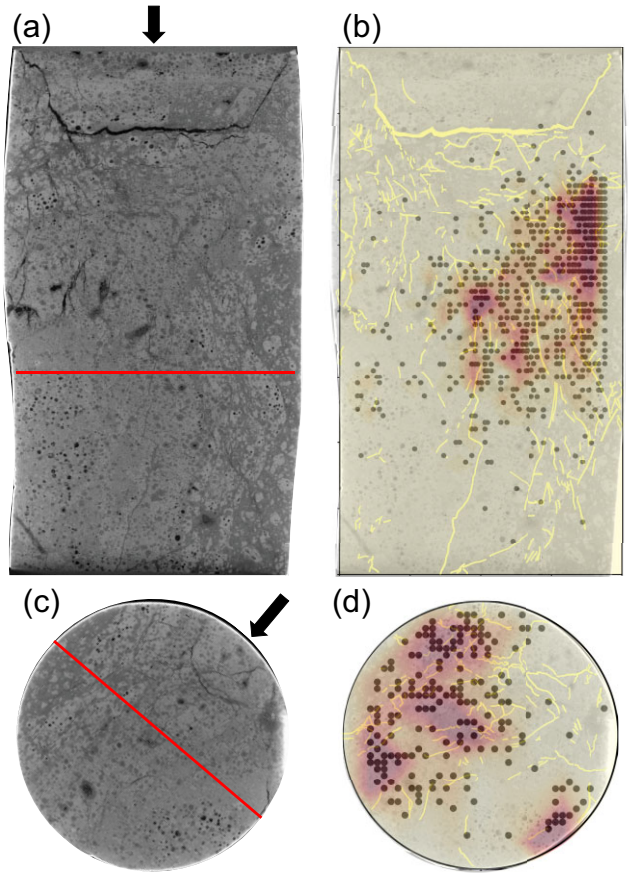

Figure 7. Cross-sections of the X-ray tomographic images of the deformed sample. (a) and (c) The raw images. (b) and (d) Images overlaid by the interpreted microfractures (yellow lines) and the heat map of the located AE events (black dots; events within 1 mm are projected). The two red lines mark the location of the radial and axial slice, and the black arrows mark the observation angle.

events (2196 out of 8791 in our case). At this step, elastic AmRTM or TRI is necessary as it represents the 'true' adjoint operation of elastic wave propagation needed for estimating the moment tensor. Focusing on fewer events of good quality, extracting the time-dependent adjoint strain fields at given source locations and picking the onset time (from one channel) becomes manageable and straightforward. The high-fidelity AE locations from GmRTM in previous stage contribute to the estimation accuracy of the moment tensors.

4.2 AE locations and focal mechanism analysis

The temporal and spatial distribution of AEs show a distributed rather than localized nature of deformation (Figs 5 and 6). The distribution of AEs towards failure are scattered across the sample and show no localized feature such as a sharp fault plane as observed in short-term failure studies, for example, Lockner *et al.* (1991) and Benson *et al.* (2007). This observation agrees with the claim of Xing *et al.* (2022) regarding a complicated and distributed fracture network rather than a well-defined localized shear fracture plane under our experimental conditions and supports the idea that brittle creep deformation under fluid-saturated conditions is accommodated by distributed deformation. The time-dependence of strain accumulation is caused by subcritical microcracking (e.g. Brantut *et al.* 2013; Mighani *et al.* 2019; Xing *et al.* 2022). The microcracking mechanism suggests that nucleation of the microcracking takes place at the natural defects/flaws within the sample (e.g. microcracks, fissures and pores; Sammis & Ashby 1986). With the seemingly random distribution of these flaws in the sample, the nucleated microcracks, some of which propagate fast enough to generate AEs, would locate in a random and distributed manner as observed. The dense clustering of AEs at heights of 30–50 mm (Fig. 5b) could be developed from the initial heterogeneous distribution of pores which act as nucleation sites for crack initiation. This clustering can be observed from the early stage of the deformation (< 24 hr of the total experiment duration), and the temporal distribution (Fig. 6) of AEs further showed that the apparent spatial clustering of AEs is randomly distributed temporally.

Although the AE location distribution is in agreement with that deduced by Xing *et al.* (2022) and implies a distributed deformation pattern during the creep, results from the focal mechanism seem to contrast the previous conclusion drawn from the microstructural observations that the creep deformation in this experiment is dominated by mode-I tensile cracking (Xing *et al.* 2022). Focal mechanism results from this study suggest a high portion of shear fracture (overall ∼41%; see Fig. 11d). This discrepancy may be explained by the crack growth and coalescence model (Myer *et al.* 1992; Bernabé & Pec 2022). As described in the 'wing-crack/sliding-crack' model, the macroscopic strain during creep is mainly accommodated by crack growth and coalescence around representative dominant microshear bands. The locations of AEs corresponding to different fracture types also show similarities where patterns of dense distribution of fractures are observed across all types of AE events and support the idea that the tensile and shear events are systematically connected. Furthermore, it is possible that mode I cracks are more prone to subcritical cracking and are therefore under-represented in the AE recordings.

The determined deformation patterns suggest that the recorded shear fractures are caused by fracture coalescence while tensile fractures are caused by wing crack propagation of the tips of the shear fractures. Shear fracture becomes the dominant type towards the end of the experiment, while the tensile fractures were the dominant type until ∼270 hr of the experiment (Fig. 11a). This interpretation proposes why shear fractures become dominant towards failure as crack density increases to a point where the sample becomes effectively saturated with cracks, that is, the generation of new cracks leads to coalescence of existing cracks. This interpretation is in agreement with previous observations that fracture coalescence increases during the stage preceding failure (e.g. Reches & Lockner 1994; Reches 1999; Stanchits *et al.* 2006; McBeck *et al.* 2021) and also implies that the proportion of shear cracks in all of the fracturing events can be used as an indicator for potential macroscopic failure prediction in addition to the existing methods using *b*-value, C integral, fractal dimension *d*, space–time event distribution, etc. (e.g. Lei & Satoh 2007; Xu *et al.* 2009; Kwiatek *et al.* 2014) during laboratory experiments and could also be useful in industrial applications for reservoir stability monitoring purposes.

5 CONCLUSIONS

To deepen our understanding of the brittle creep deformation of a basalt sample from the Carbfix site (Iceland) in presence of CO_2-rich fluids, we located the 8791 detected AE events using a cross-correlation-based source imaging method named GmRTM. The resulting image cubes showed significantly fewer imaging artefacts

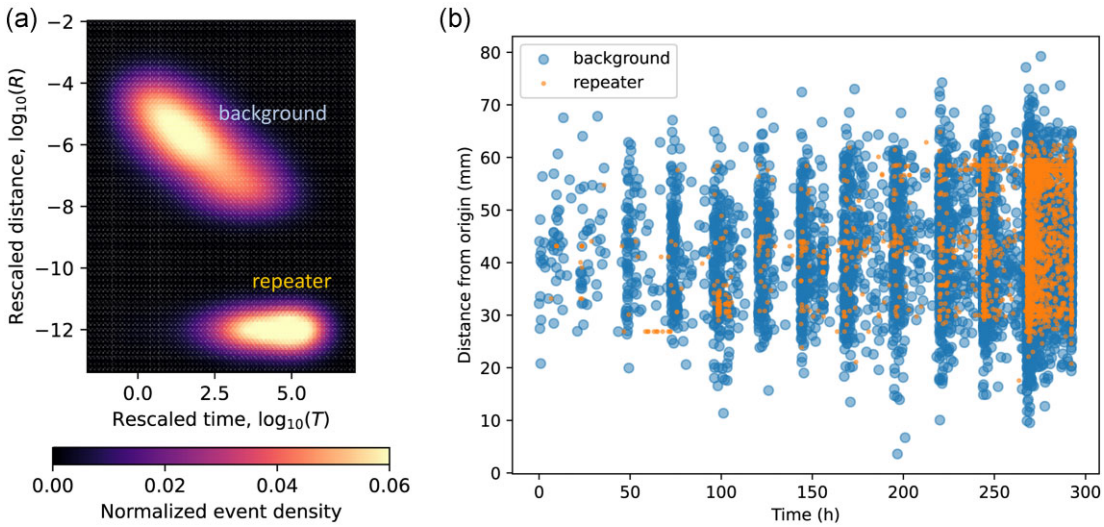

Figure 8. Two clusters of AE events (background events and repeaters) determined by the nearest-neighbour analysis in the (a) time increment (T)–spatial increment (R) domain and in the conventional (b) time (t)–space (x) domain. Here, the tempo-spatial increment T and R indicate the duration and distance of two events respectively, while t and x are compared to the original time and spatial coordinate.

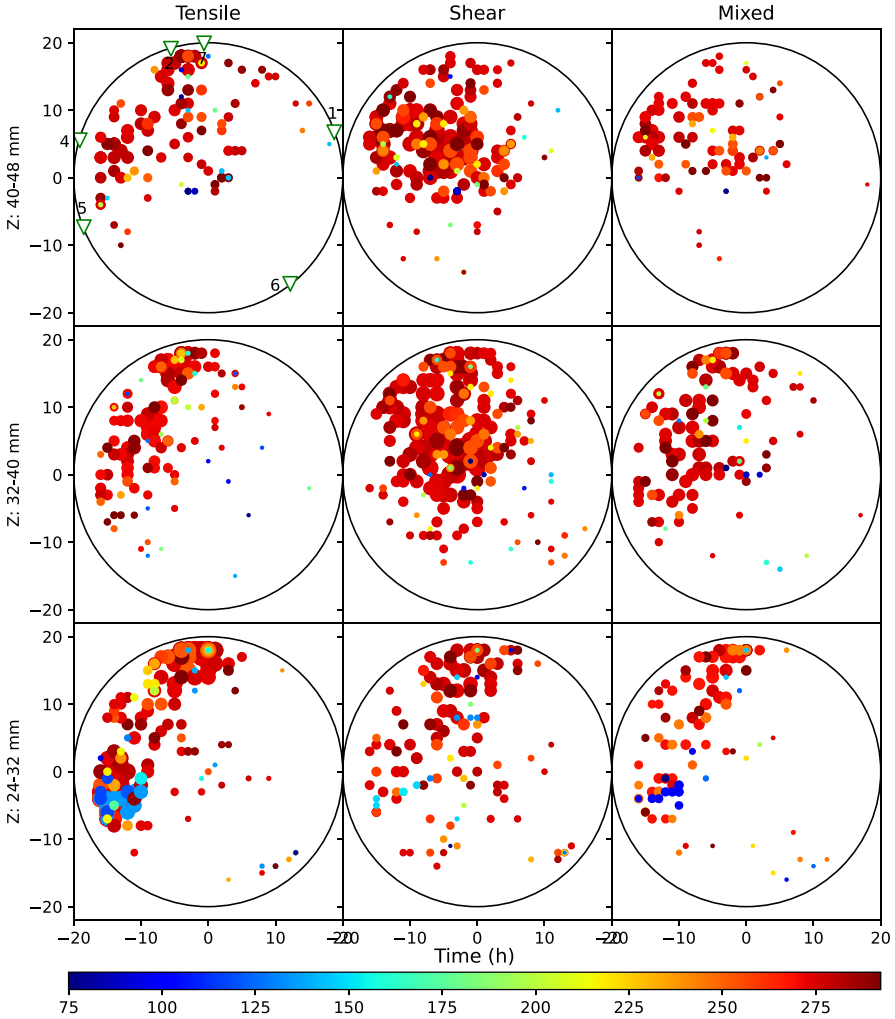

Figure 9. AE distribution corresponding to different crack types and height bins. The colours and sizes of the dots mark time evolution and density of the distribution, respectively.

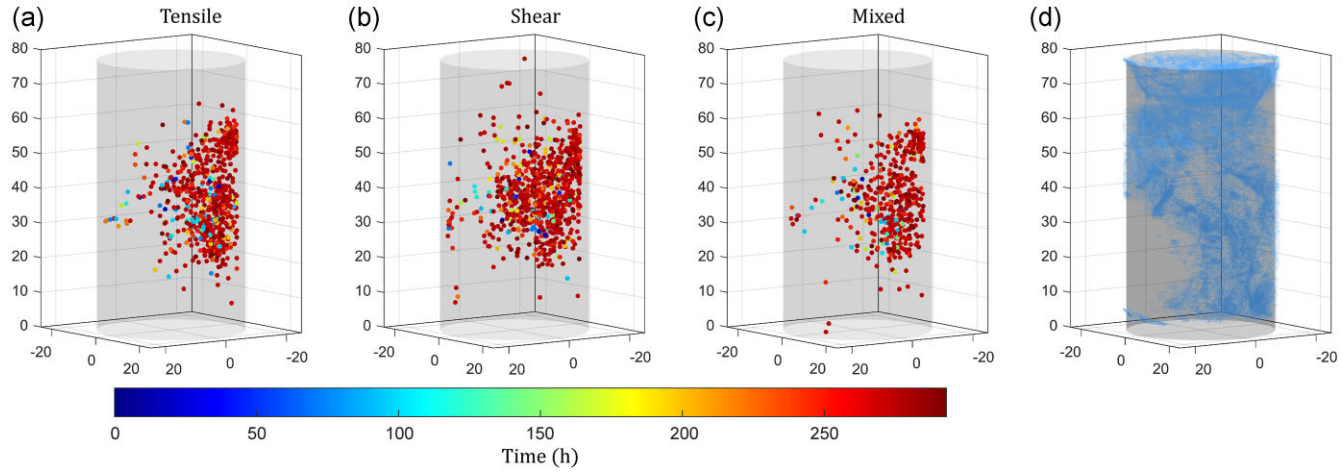

Figure 10. Distributions of AEs corresponding to (a) tensile, (b) shear and (c) mixed crack types, with colour encoding the total (all 12 stages) evolving time. (d) Fracture and porosity networks thresholded from the X-ray tomographic image of the deformed sample highlighted in blue.

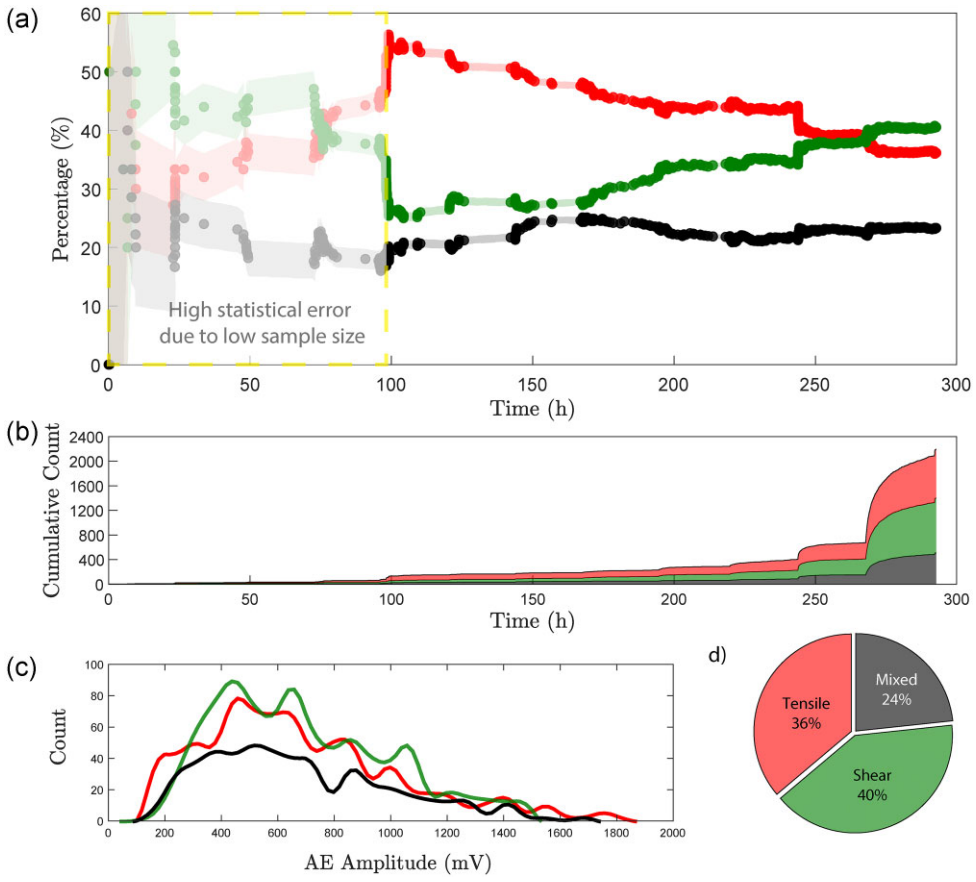

Figure 11. Time evolution of the cumulative (a) percentage and (b) counts of AEs corresponding different crack types (red: tensile; green: shear and black: mix-type). (c) Smoothed histograms of the maximum amplitudes of the selected 2196 events (for focal mechanism analysis) grouped by the fracture type. (d) Pie chart implying the proportions of different crack types among the selected 2196 AE events.

and required no excitation time estimation compared to conventional TRI. The estimated source locations were in general agreement with microstructural observations from X-ray computed tomography and showed a scattered distribution, supporting that the creep deformation under our experimental conditions favours distributed deformation due to subcritical microcracking. However, further clustering study of the tempo-spatial AE distributions using the nearest-neighbour approach suggests a group of 'repeaters' which are events spatially co-located with preceding events that likely imply the growth of existing cracks.

Next, we selected a subset of 2196 AE events with high SNR, and applied elastic time reversal for moment tensor estimation. The

AE events were categorized as tensile-, shear-, and mixed-cracks based on the moment tensor decomposition. Different types of AEs displayed similarly dispersed spatial distribution and statistical amplitude distribution, suggesting that tensile and shear cracks might be connected systematically as described in the growing shear band model derived from the classical 'wing-crack' model. Temporally, shear events outnumbered tensile cracking starting from the last loading stages, indicating shear fracture coalescing towards ultimate failure. The nearest-neighbour analysis also supports our interpretation that events occurring at later stage of the experiment show high correlations in location ('repeaters') which indicates reactivation or propagation of previously developed cracks.

Our AE location and focal mechanism analysis support the 'wing-crack' model for crack propagation and coalescence during brittle creep deformation under fluid-saturated conditions: the estimated focal mechanisms reveal the dominance of tensile cracks before crack coalescence, which is consistent with the 'wing-crack' model where the tensile cracks initiate as shear fracture slide. The AE observations suggested that the brittle creep deformation occurs in an overall distributed manner.

ACKNOWLEDGMENTS

We thank Malcolm C. A White, Hoagy O'Ghaffari and Hongrui Qiu for helpful discussions, and Uli Mok for technical assistance in the laboratory. The reviews by the editors Dr Christoph Sens-Schönfelder and Dr Jörg Renner, Dr Georg Dresen and another anonymous referee helped us improve the manuscript. Most of the computation is conducted using the Vector Engine cluster SX-Aurora TSUBASA (VE card: Type20B) from the NEC cooperation (www.nec.com), with the technique support from Yoshiyuki Kubo (NEC). We would also like to acknowledge the computational resources provided by the OU Supercomputing Center for Education & Research (OSCER) at the University of Oklahoma (OU). Additionally, we extend our gratitude for the 'CORD' Laboratory technician support by NSF-2054414 and funding by MIT's 'Advanced Carbon Mineralization Initiative'. NN is partly supported by the U.S. Department of Energy under award number DE-AC02–05CH11231 for this study.

DATA AVAILABILITY

The AE waveform data and sample source code for moment tensor estimation are available at 10.5281/zenodo.10584481.

SUPPORTING INFORMATION

Supplementary data are available at *GJI* online.

suppl_data

Please note: Oxford University Press is not responsible for the content or functionality of any supporting materials supplied by the authors. Any queries (other than missing material) should be directed to the corresponding author for the paper.

REFERENCES

Akazawa, T., 2004. A technique for automatic detection of onset time of P-and S-phases in strong motion records, in *Proc. of the 13th World Conf. on Earthquake Engineering,* Vol. **786,** p. 786, Vancouver, Canada.

Aker, E., Kühn, D., Vavryčuk, V., Soldal, M. & Oye, V., 2014. Experimental investigation of acoustic emissions and their moment tensors in rock during failure, *Int. J. Rock. Mech. Min. Sci.,* **70,** 286–295.

Alfredsson, H., Hardarson, B., Franzson, H. & Gíslason, S.R., 2008. Co2 sequestration in basaltic rock at the hellisheidi site in sw iceland: stratigraphy and chemical composition of the rocks at the injection site, *Mineral. Mag.,* **72**(1), 1–5.

Aradóttir, E., Sonnenthal, E., Björnsson, G. & Jónsson, H., 2012. Multidimensional reactive transport modeling of co2 mineral sequestration in basalts at the hellisheidi geothermal field, iceland, *Int. J. Greenhouse Gas Control,* **9,** 24–40.

Artman, B., Podladtchikov, I. & Witten, B., 2010. Source location using time-reverse imaging, *Geophys. Prospect.,* **58**(5), 861–873.

Ashby, M. & Sammis, C., 1990. The damage mechanics of brittle solids in compression, *Pure appl. Geophys.,* **133,** 489–521.

Atkinson, B.K. & Meredith, P.G., 1987. The theory of subcritical crack growth with applications to minerals and rocks, *Fract. Mech. Rock,* **2,** 111–166.

Bai, T., Lyu, B., Li, F., Williamson, P. & Nakata, N., 2022a. Elastic geometric-mean reverse time migration for source imaging, *Geophysics,* **87**(4), KS135–KS146.

Bai, T., Lyu, B., Williamson, P. & Nakata, N., 2022b. Receiver grouping strategies for hybrid geometric-mean reverse time migration, *Geophysics,* **87**(2), KS45–KS55.

Baud, P. & Meredith, P., 1997. Damage accumulation during triaxial creep of darley dale sandstone from pore volumometry and acoustic emission, *Int. J. Rock. Mech. Min. Sci.,* **34**(3–4), 24–e1.

Benson, P.M., Thompson, B.D., Meredith, P.G., Vinciguerra, S. & Young, R.P., 2007. Imaging slow failure in triaxially deformed Etna basalt using 3D acoustic-emission location and X-ray computed tomography, *Geophys. Res. Lett.,* **34**(3), doi: 10.1029/2006GL028721.

Bernabé, Y. & Pec, M., 2022. Brittle creep and failure: a reformulation of the wing crack model, *J. geophys. Res.: Solid Earth,* **127**(9), doi: 10.1029/2022JB024610.

Brantut, N., 2018. Time-resolved tomography using acoustic emissions in the laboratory, and application to sandstone compaction, *J. geophys. Int.,* **213**(3), 2177–2192.

Brantut, N., Baud, P., Heap, M. & Meredith, P., 2012. Micromechanics of brittle creep in rocks, *J. geophys. Res.: Solid Earth,* **117**(B8). doi: 10.1029/2012JB009299.

Brantut, N., Heap, M., Meredith, P. & Baud, P., 2013. Time-dependent cracking and brittle creep in crustal rocks: a review, *J. Struct. Geol.,* **52,** 17–43.

Chang, S.-H. & Lee, C.-I., 2004. Estimation of cracking and damage mechanisms in rock under triaxial compression by moment tensor analysis of acoustic emission, *Int. J. Rock. Mech. Min. Sci.,* **41**(7), 1069–1086.

Claerbout, J., 2014. *Geophysical image estimation by example,* Lulu. com.

Dong, L., Hu, Q., Tong, X. & Liu, Y., 2020. Velocity-free ms/ae source location method for three-dimensional hole-containing structures, *Engineering,* **6**(7), 827–834.

Fichtner, A., Bunge, H.-P. & Igel, H., 2006. The adjoint method in seismology: I. theory, *Phys. Earth planet. Inter.,* **157**(1–2), 86–104.

Finger, C. & Saenger, E.H., 2021. Determination of the time-dependent moment tensor using time reverse imaging, *Geophysics,* **86**(2), KS63–KS77.

Fink, M., 1997. Time reversed acoustics., *Phys. Today,* **50**(3), 34–40.

Ghaffari, H. & Pec, M., 2020. An ultrasound probe array for a high-pressure, high-temperature solid medium deformation apparatus, *Rev. Sci. Instrum.,* **91**(8), doi: 10.1063/5.0004035.

Ghaffari, H., Mok, U. & Pec, M., 2021. On calibration of piezoelectric sensors with laser doppler vibrometer, *J. acoust. Soc. Am.,* **150**(4), 2503–2513.

Gharti, H.N., Oye, V., Kühn, D. & Zha, P., 2011. Simultaneous microearthquake location and moment-tensor estimation using time-reversal imaging, in *2011 SEG Annual Meeting,* OnePetro, 1632

Gislason, S.R. *et al.*, 2010. Mineral sequestration of carbon dioxide in basalt: a pre-injection overview of the carbfix project, *Int. J. Greenhouse Gas Control,* **4**(3), 537–545.

Goebel, T., Becker, T., Schorlemmer, D., Stanchits, S., Sammis, C., Rybacki, E. & Dresen, G., 2012. Identifying fault heterogeneity through mapping spatial anomalies in acoustic emission statistics, *J. geophys. Res.: Solid Earth,* **117**(B3), doi: 10.1029/2011JB008763.

Goodman, R.E., 1963. Subaudible noise during compression of rocks, *Bull. geol. Soc. Am.,* **74**(4), 487–490.

Graham, C.C., Stanchits, S., Main, I.G. & Dresen, G., 2010. Comparison of polarity and moment tensor inversion methods for source analysis of acoustic emission data, *Int. J. Rock. Mech. Min. Sci.,* **47**(1), 161–169.

Heap, M., Baud, P., Meredith, P., Vinciguerra, S., Bell, A. & Main, I., 2011. Brittle creep in basalt and its application to time-dependent volcano deformation, *Earth planet. Sci. Lett.,* **307**(1–2), 71–82.

Jarillo Michel, O. & Tsvankin, I., 2017. Waveform inversion for microseismic velocity analysis and event location in vti media, *Geophysics,* **82**(4), WA95–WA103.

Jia, S.Q., Wong, R.C. & Eaton, D.W., 2022. Characterization of damage processes in montney siltstone under triaxial compression using acoustic emission and diagnostic imaging, *J. geophys. Int.,* **228**(3), 2005–2017.

Kawakatsu, H. & Montagner, J.-P., 2008. Time-reversal seismic-source imaging and moment-tensor inversion, *J. geophys. Int.,* **175**(2), 686–688.

Kiyoo, M., 1962. Study of elastic shocks caused by the fracture of heterogeneous materials and its relations to earthquake phenomena, in *Bulletin of the Earthquake Research Institute,* pp. 125–173, University of Tokyo, Tokyo, Japan.

Kwiatek, G., Goebel, T. & Dresen, G., 2014. Seismic moment tensor and b value variations over successive seismic cycles in laboratory stick-slip experiments, *Geophys. Res. Lett.,* **41**(16), 5838–5846.

Lackner, K.S., Wendt, C.H., Butt, D.P., Joyce, E.L. Jr & Sharp, D.H., 1995. Carbon dioxide disposal in carbonate minerals, *Energy,* **20**(11), 1153–1170.

Lei, X. & Satoh, T., 2007. Indicators of critical point behavior prior to rock failure inferred from pre-failure damage, *Tectonophysics,* **431**(1–4), 97–111.

Lei, X., Kusunose, K., Rao, M., Nishizawa, O. & Satoh, T., 2000. Quasi-static fault growth and cracking in homogeneous brittle rock under triaxial compression using acoustic emission monitoring, *J. geophys. Res.: Solid Earth,* **105**(B3), 6127–6139.

Lockner, D., 1993. The role of acoustic emission in the study of rock fracture, *Int. J. Rock. Mech. Min. Sci. Geomech. Abstr.,* **30,** 883–899

Lockner, D., Byerlee, J., Kuksenko, V., Ponomarev, A. & Sidorin, A., 1991. Quasi-static fault growth and shear fracture energy in granite, *Nature,* **350**(6313), 39–42.

Lockner, D., Byerlee, J., Kuksenko, V., Ponomarev, A. & Sidorin, A., 1992. Observations of quasistatic fault growth from acoustic emissions, in *International Geophysics,* Vol. **51,** pp. 3–31, Elsevier. Evans, Brian & Wong, Teng-fong.

Manthei, G., 2005. Characterization of acoustic emission sources in a rock salt specimen under triaxial compression, *Bull. seism. Soc. Am.,* **95**(5), 1674–1700.

Manthei, G. & Eisenblätter, J., 2008. Acoustic emission in study of rock stability, in *Acoustic Emission Testing: Basics for Research-Applications in Civil Engineering,* pp. 239–310. Springer Nature. U., Christian, Ohtsu, Masayasu, G., Dimitrios & Tomoki, Shiotani.

Matter, J.M. & Kelemen, P.B., 2009. Permanent storage of carbon dioxide in geological reservoirs by mineral carbonation, *Nat. Geosci.,* **2**(12), 837–841.

Matter, J.M. *et al.*, 2016. Rapid carbon mineralization for permanent disposal of anthropogenic carbon dioxide emissions, *Science,* **352**(6291), 1312–1314.

McBeck, J.A., Zhu, W. & Renard, F., 2021. The competition between fracture nucleation, propagation, and coalescence in dry and water-saturated crystalline rock, *Solid Earth,* **12**(2), 375–387.

Meredith, P. & Atkinson, B., 1983. Stress corrosion and acoustic emission during tensile crack propagation in whin sill dolerite and other basic rocks, *J. geophys. Int.,* **75**(1), 1–21.

Mighani, S., Bernabé, Y., Boulenouar, A., Mok, U. & Evans, B., 2019. Creep deformation in vaca muerta shale from nanoindentation to triaxial experiments, *J. geophys. Res.: Solid Earth,* **124**(8), 7842–7868.

Myer, L., Kemeny, J.M., Zheng, Z., Suarez, R., Ewy, R. & Cook, N., 1992. Extensile cracking in porous rock under differential compressive stress, *Appl. Mech. Rev.,* **45**(8), 263–280.

Nakata, N. & Beroza, G.C., 2015. Reverse-time migration for microseismic sources using the geometric mean as an imaging condition, in *SEG Technical Program Expanded Abstracts 2015,* pp. 2451–2455, Society of Exploration Geophysicists.

Nakata, N. & Beroza, G.C., 2016. Reverse time migration for microseismic sources using the geometric mean as an imaging condition, *Geophysics,* **81**(2), KS51–KS60.

O'Ghaffari, H., Peč, M., Mittal, T., Mok, U., Chang, H. & Evans, B., 2023. Microscopic defect dynamics during a brittle-to-ductile transition, *Proc. Natl. Acad. Sci.,* **120**(42), e2305667120. doi: 10.1073/pnas.230566712.

Ohtsu, M., 1991. Simplified moment tensor analysis and unified decomposition of acoustic emission source: application to in situ hydrofracturing test, *J. geophys. Res.: Solid Earth,* **96**(B4), 6211–6221.

Petružálek, M., Jechumtálová, Z., Kolář, P., Adamová, P., Svitek, T., Šílenỳ, J. & Lokajíček, T., 2018. Acoustic emission in a laboratory: Mechanism of microearthquakes using alternative source models, *J. geophys. Res.: Solid Earth,* **123**(6), 4965–4982.

Plessix, R.-E., 2006. A review of the adjoint-state method for computing the gradient of a functional with geophysical applications, *J. geophys. Int.,* **167**(2), 495–503.

Reches, Z., 1999. Mechanisms of slip nucleation during earthquakes, *Earth planet. Sci. Lett.,* **170**(4), 475–486.

Reches, Z. & Lockner, D.A., 1994. Nucleation and growth of faults in brittle rocks, *J. geophys. Res.: Solid Earth,* **99**(B9), 18159–18173.

Sammis, C. & Ashby, M., 1986. The failure of brittle porous solids under compressive stress states, *Acta Metall.,* **34**(3), 511–526.

Scholz, C., 1968. Experimental study of the fracturing process in brittle rock, *J. geophys. Res.,* **73**(4), 1447–1454.

Snæbjörnsdóttir, S.Ó. & Gislason, S.R., 2016. Co2 storage potential of basaltic rocks offshore iceland, *Energy Proc.,* **86,** 371–380.

Stanchits, S., Vinciguerra, S. & Dresen, G., 2006. Ultrasonic velocities, acoustic emission characteristics and crack damage of basalt and granite, *Pure appl. Geophys.,* **163,** 975–994.

Sun, J., Zhu, T., Fomel, S. & Song, W.-Z., 2015. Investigating the possibility of locating microseismic sources using distributed sensor networks, in *SEG Technical Program Expanded Abstracts 2015,* pp. 2485–2490, Society of Exploration Geophysicists.

Tromp, J., Tape, C. & Liu, Q., 2005. Seismic tomography, adjoint methods, time reversal and banana-doughnut kernels, *J. geophys. Int.,* **160**(1), 195–216.

Vavryčuk, V., 2015. Moment tensor decompositions revisited, *J. Seismol.,* **19,** 231–252.

Virieux, J. & Operto, S., 2009. An overview of full-waveform inversion in exploration geophysics, *Geophysics,* **74**(6), WCC1–WCC26.

Vlček, J., Fischer, T. & Vilhelm, J., 2016. Back-projection stacking of p- and s-waves to determine location and focal mechanism of microseismic events recorded by a surface array, *Geophys. Prospect.,* **64**(6), 1428–1440.

Xing, T., Ghaffari, H.O., Mok, U. & Pec, M., 2022. Creep of carbfix basalt: influence of rock–fluid interaction, *Solid Earth,* **13**(1), 137–160.

Xu, J., Tang, X., Li, S., Tao, Y. & Jiang, Y., 2009. Space-time evolution rules study on acoustic emission location in rock under cyclic loading, *Front. Archit. Civil Eng. China,* **3,** 422–427.

Zaliapin, I. & Ben-Zion, Y., 2020. Earthquake declustering using the nearest-neighbor approach in space-time-magnitude domain, *J. geophys. Res.: Solid Earth,* **125**(4), e2018JB017120. doi: 10.1029/2018JB017120.

Zang, A., Christian Wagner, F., Stanchits, S., Dresen, G., Andresen, R. & Haidekker, M.A., 1998. Source analysis of acoustic emissions in aue granite cores under symmetric and asymmetric compressive loads, *J. geophys. Int.,* **135**(3), 1113–1130.

Zhang, Z., White, M.C., Bai, T., Qiu, H. & Nakata, N., 2023. Characterizing microearthquakes induced by hydraulic fracturing with hybrid borehole das and three-component geophone data, *IEEE Trans. Geosci. Remote Sens.,* **61,** 1–15.